Eur. J. Mech. B - Fluids 20 (2001) 255–274

S0997-7546(00)01111-0/FLA

Electromagnetic control of seawater flow around circular cylinders

Oliver Posdziech *, Roger Grundmann

[a] *Institute for Aerospace Engineering, Department of Mechanical Engineering, Dresden University of Technology, 01062 Dresden, Germany*

(Received 10 December 1999; revised 13 June 2000; accepted 16 August 2000)

Abstract – We investigate numerically the electromagnetic control of seawater flows over an infinitely long circular cylinder. Stripes of electrodes and magnets, wrapped around the cylinder surface, produce a tangential body force (Lorentz force) that stabilizes the flow. This mechanism delays flow separation, reduces drag and lift, and finally suppresses the von Kármán vortex street. Results from two-dimensional simulations of the Navier–Stokes equations in a range $10 < Re < 300$ and Lorentz force calculations are presented. Emphasis is placed on the disclosure of physical phenomena as well as a quantitative detection of the flow field and forces. It is shown that the drag strongly depends on the geometry of the electromagnetic actuator and on its location at the cylinder surface. The effect of flow control increases with larger Reynolds numbers, since the boundary layer thickness and the penetration depth of the Lorentz force are closely connected. © 2001 Éditions scientifiques et médicales Elsevier SAS

electromagnetic flow control / seawater / circular cylinder

1. Introduction

Active or passive methods to reduce the drag in external flows possess an enormous technological importance. Flow control is managed by physical mechanisms like transition delay, separation postponement, or damping of turbulence in boundary layers. Electrically conducting fluids can be controlled by means of electromagnetic forces. Even if the conductivity is very modest (e.g. seawater $\sigma = 5$–6 S/m), crossed electric and magnetic fields are able to produce a Lorentz force to alter the flow structure near the surface. A possible configuration to generate a streamwise Lorentz force by means of stripes of electrodes and magnets on a flat plate is shown in *figure 1*. The method can be applied to reduce frictional as well as pressure drag of sea ships or submarines by altering the turbulence production in the boundary layer or preventing flow separation. The high Reynolds number range of practical applications is not accessible to direct numerical simulations. Therefore, fundamental effects are studied at low *Re* and simple geometries. The advantage of this control method is its acting in the volume and the absence of moving parts leading to interactions between flow and actuator. Unlike ordinary magneto-hydro-dynamics (MHD), the induced current density is negligible so one has to apply an external electrical field to interact with the magnetic flux. This special application of MHD is usually called electro-magneto-hydro-dynamics (EMHD) or electro-magnetic-flow-control (EMFC). We will use the latter expression throughout the article.

The proposal of using stripes of electrodes and magnets to prevent boundary layer growth in seawater was made in the sixties in Riga, Latvia [1]. The classical ideas were resumed one decade ago, as the postponement of flow separation on a circular cylinder with crossed electric and magnetic fields was shown by Tsinober [2]. Nosenchuck and Brown [3] measured a reduction of skin friction of up to 90% by means of

* Correspondence and reprints.
E-mail address: posdzie@tfd.mw.tu-dresden.de (O. Posdziech).

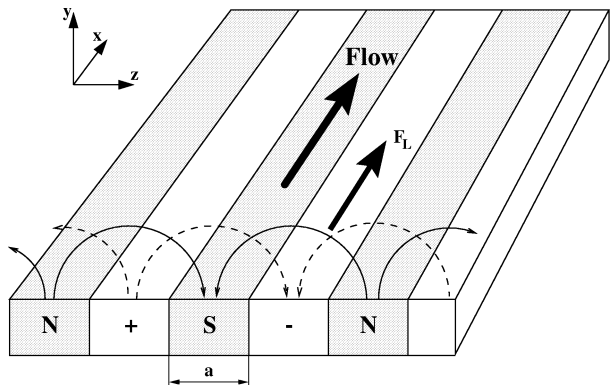

Figure 1. Generation of a Lorentz force F_L by means of crossed electric and magnetic fields on a flat plate.

chessboardlike arranged electrodes/magnets to induce a wall-normal Lorentz force in a flat plate boundary layer. The injection of an electrolyte generated a non-uniform electrical conductivity. Afterwards, several research groups have investigated experimentally or numerically EMFC mainly on the turbulent boundary layer. They used either 'stripes', alternating pairs of electrodes/magnets to induce a streamwise Lorentz force [4,5], or a chessboardlike arrangement in order to get a wall-normal force called 'tiles' [6,7]. Recently, a spanwise oscillating Lorentz-force (see Berger et al. [8]) was successfully used to reduce the skin friction in a turbulent boundary layer. A considerable scatter of results was found even on very similar arrangements. This could result from inadequate calculations of the Lorentz force in numerics or difficulties with established measurement techniques. Clear evidence of whether the technique of electromagnetic drag reduction in seawater does indeed lead to a reduction of surface integrated viscous drag or not, is lacking so far.

Within this work, the simpler approach to stabilize the boundary layer in order to prevent separation is tackled. The control of flow separation has in contrast to the turbulent boundary layer control some advantages in terms of fundamental studies: (1) the physical mechanism of control is obvious namely the prevention of an inflectional velocity profile; (2) numerical simulations as well as experiments are easier to perform and to compare; (3) the effect of flow control can be shown simply through visualizations. Some experimental results can be found in Weier et al. [9,10]. The flow around an infinitely long circular cylinder is chosen as testcase to study the flow separation on bluff bodies. It has attracted researchers for more than a century since many physical phenomena, also relevant for more complicated geometries, occur in a small range of Reynolds numbers. We will concentrate on the low Reynolds number scope and assume a two-dimensional flow which is justified for $Re \leqslant 190$ in the uncontrolled case.

In section 2, we show the assumption of a Lorentz force tangential to the cylinder surface, and how it is included in the numerical investigations. The numerical scheme as well as a code validation by means of experimental and numerical results are presented in section 3. Afterwards, effects of width of electrodes and magnets (responsible for the penetration depth of the Lorentz force), strength of forcing, and location of imposing at constant Reynolds number are shown in section 4. The influence of the Reynolds number on the drag reduction mechanism is presented in section 5. Finally, the postponement of instability of stationary flow, connected with a suppression of the von Kármán vortex street, is presented in section 6.

2. Tangential Lorentz force on an infinitely long circular cylinder

Stripes of alternating electrodes and magnets generate a streamwise (perpendicular to the electric and magnetic field) volumetric force called Lorentz force (see *figure 1*). The Lorentz force per unit volume in an electrically conducting medium of conductivity σ is given by

$$\mathbf{F_L} = \mathbf{J} \times \mathbf{B}, \tag{1}$$

where **J** is the current density and **B** is the magnetic induction. Ohm's law applied to moving fluids is represented by

$$\mathbf{J} = \sigma(\mathbf{E} + \mathbf{U} \times \mathbf{B}) \tag{2}$$

with **E** the externally aligned electric field. One fundamental quantity of MHD is the magnetic Reynolds number as ratio between the characteristic time for magnetic diffusion and the transit time of fluid particles

$$Re_m = \mu\sigma U L. \tag{3}$$

With μ the magnetic permeability of seawater ($\mu \approx \mu_0$), σ the electrical conductivity, U the free-stream velocity, and L the cylinder diameter as characteristic length, the magnetic Reynolds number is in the order of $Re_m \approx 5 \cdot 10^{-12} Re$. In that case, the magnetic field is not influenced by the velocity field, and can be calculated as if the fluid was at rest. So equation (2) becomes

$$\mathbf{J} = \sigma \mathbf{E}. \tag{4}$$

Unlike ordinary MHD, we can calculate the Lorentz force decoupled from the Navier–Stokes equations. The calculation of electric and magnetic fields follows the description in Berger et al. [8]. The field and Lorentz force distributions are shown there.

In this work, the calculation of electric and magnetic fields have been performed by means of the finite element code OPERA, that numerically solves the Maxwell equations. On the assumption of infinite long electrodes and magnets in the streamwise direction (edge effects are neglected), the problem is simplified as two-dimensional. The magnetic induction is dependent on the height of magnets in the wall-normal direction. For $H \to \infty$, the mean induction amounts to $\overline{B}_0 = 1/2 M_0$ with M_0 the magnetization of permanent magnets. The height of the magnets has been varied in the numerical investigation in order to approach the asymptotic value. Both fields have a singularity on the passage between electrodes and magnets. This results in a wavy Lorentz force distribution in the spanwise direction. Far from the surface, the waviness diminishes, but the force takes very low values. The behavior in wall-normal direction is shown in *figure 2* where the Lorentz force is plotted for different widths a (solid line). The Lorentz force exponentially decays in all cases. A configuration with $a = 2$ mm has considerably higher values at the surface, but the force decreases faster away from the wall compared to wider electrodes/magnets. The integral $\int F_L(y)\,\mathrm{d}y$ is identical for all widths. So, from an energetical point of view, it makes no difference whether the electrodes are 2 mm or 20 mm wide, assuming a large number of spanwise stripes.

For two-dimensional calculations, only a mean force profile $F_L(y)$, with y the coordinate in the wall-normal direction, is included in the solution of the Navier–Stokes equations

$$F_L(y) = J_0 B_0 g(\phi) \mathrm{e}^{-\frac{\pi}{a} y}, \quad g(\phi) = \begin{cases} 1, & \phi_0 \leqslant \phi \leqslant \phi_1, \\ -1, & 180^\circ + \phi_0 \leqslant \phi \leqslant 180^\circ + \phi_1, \\ 0, & \text{elsewhere} \end{cases} \tag{5}$$

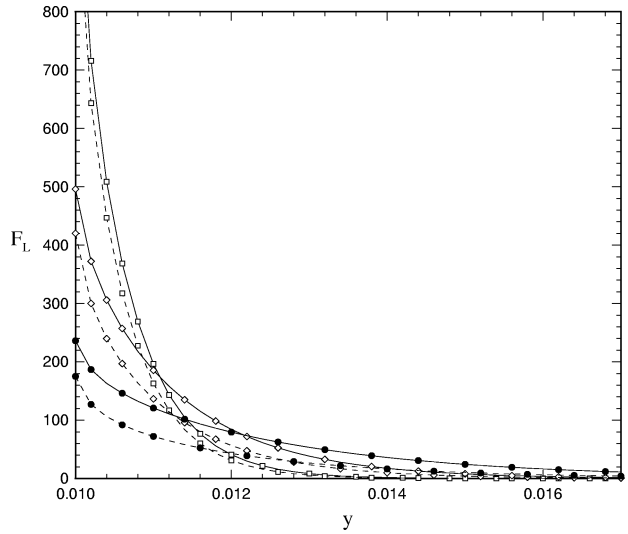

Figure 2. Comparison of flat plate and cylinder approximation of Lorentz force in the wall-normal direction for different widths a of electrodes/magnets: □, $a = 2$ mm; ◇, $a = 4$ mm; •, $a =$ mm (——, flat plate; – – –, cylinder diameter $D = 20$ mm).

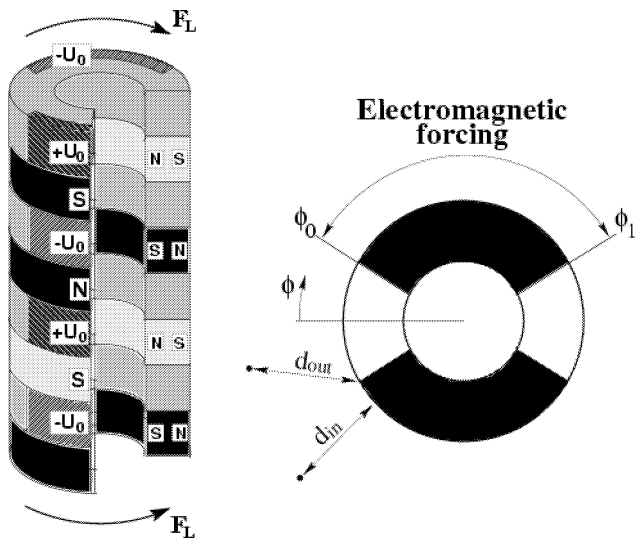

Figure 3. Generation of a Lorentz force on a circular cylinder.

with J_0 the mean current density and B_0 the mean magnetic induction at the wall. The term a describes the width of electrodes resp. magnets, it acts as penetration depth of the Lorentz force.

Figure 3 shows a circular cylinder with alternating electrodes and magnets in order to impose a Lorentz force in the surrounding fluid. The FEM-code has been used to perform an axisymmetric solution for the electromagnetic fields in cylindrical coordinates. *Figure 2* shows the comparison between the force profiles over the plate and the cylinder. The Lorentz force decays exponentially for both geometries. However, the force is lowered with the width of electrodes/magnets due to the influence of curvature. In the following, we will assume the flat plate solution for infinite electrodes/magnets in order to generalize the separation control approach. The cylinder flow serves as canonical testcase for the control, since it is well documented in literature. Real

applications (e.g. hydrofoils) are much less affected by the errors introduced due to the curvature of the surface. The investigation is extended to widths a where the deviation from the flat plate solution increases. Performing the parameter study to smaller a, would result in numerical problems in connection with the resolution of the near-wall force. In addition, the practical realization of the Lorentz force distribution in an experiment is not the topic of this numerical study. For instance, a spanwise constant electromagnetic force could be generated by using special shaped electrodes.

Throughout the investigations, the covering of the cylinder surface with electrodes/magnets is varied, We define angles ϕ_0 and ϕ_1, measured from the front stagnation point, as shown in *figure 3*. The control area is always mirrored to angles $\phi > 180°$ throughout this study. Equation (5) is used to calculate the Lorentz force versus distance (d_{in}) normal to the cylinder wall, if the point in the flow field is situated within the control area $\phi_0 < \phi < \phi_1$. End effects of the electromagnetic system are neglected within the simulations, but in order to avoid a discontinuity on ϕ_0 resp. ϕ_1, equation (5) is also applied to calculate a force outside the control area. Now, the length (d_{out} in *figure 3*) is taken as distance from the last controlled point at the surface (corresponding to ϕ_0 resp. ϕ_1). Because of the exponentially character of the Lorentz force profile, the calculated force gets very small a few length units away from the control area, but guarantees a smooth distribution.

One important parameter, known from classical MHD, is the interaction parameter N as relation of electromagnetic forces to the inertial forces of the flow. We write this parameter in the form

$$N = \frac{J_0 B_0 D}{\rho U_\infty^2} \tag{6}$$

with D the diameter of the cylinder as characteristic length. In contrast to earlier publications on EMFC, we define a geometry parameter G as

$$G = \frac{a}{D} \tag{7}$$

to take into account the effect of the configuration on the flow through different profiles of Lorentz forces. The parameter N only contains the maximum force at the wall, whereas the manner of decrease in normal direction is neglected. In order to compare calculations with different geometry parameters, the product $N \cdot G$ is used. This term can be considered as integral over the wall-normal Lorentz force distribution. It is called 'scaled interaction parameter' in the following. The scaled interaction parameter would be obtained if the width a is used as characteristic length in the definition of N. Throughout the study, only steady Lorentz forces were considered. Tests with a time-dependent forcing in the scope of an unsteady flow did not result in a larger drag reduction.

3. Numerical procedure and code validation

The governing equations for a Newtonian, incompressible, and time-dependent flow problem with constant properties are the continuity equation

$$\nabla \cdot \mathbf{u} = 0 \tag{8}$$

and the momentum equations

$$\frac{\partial \mathbf{u}}{\partial t} + (\mathbf{u} \cdot \nabla)\mathbf{u} = -\frac{1}{\rho}\nabla p + \nu \nabla^2 \mathbf{u} + \mathbf{F}(y), \tag{9}$$

where **u** represents the flow velocity, p the pressure, ν the (constant) kinematic viscosity, ρ the (constant) density, and the term $\mathbf{F}(y)$ the Lorentz force per unit volume defined in equation (5), calculated decoupled from the numerical solution of the Navier–Stokes equations.

A spectral element method is used to discretize equations (8) and (9). This method combines the generality of finite element methods in handling complex geometries with the fast convergence and high accuracy of global spectral models. A three-step splitting scheme for the linear diffusion, nonlinear advection, and pressure operators is applied to write the Navier–Stokes equations in a semi-discrete form. The Lorentz force has been added to the nonlinear term. Time integration is performed by means of a mixed explicit/implicit stiffly-stable scheme of order J, where J is up to third order [11]. Further details of the code can be found in Henderson and Karniadakis [12].

Although a physically nonconfined cylinder is viewed, the discretized equations require finite boundaries in the far field. Boundary conditions along the outer edges of the computational domain are uniform flow ($u = 1, v = 0$) across the inflow, top and bottom boundaries, and outflow ($(\mathbf{n} \cdot \nabla)\mathbf{u} = 0$) downstream from the cylinder. The pressure is set to zero at the outflow boundary, along the other boundaries a high-order pressure condition of Neumann-type is used to control divergence errors introduced by the splitting scheme [11]. At the surface of the cylinder, the fluid velocity satisfies the no-slip condition with the velocity set to zero ($u = 0, v = 0$).

The code has been tested on the two-dimensional, laminar flow around a circular cylinder at low Reynolds numbers without external forcing. *Figure 4* shows an example of a spectral element mesh around the cylinder. Important geometrical parameters are the inflow length (l_i), extension of top/bottom boundaries (l_b), and outflow length (l_o). These quantities, as well as the number of elements and order of polynomial basis were varied in order to avoid blockage effects and to guarantee a sufficient resolution to catch the flow physics. Finally, a mesh with 186 spectral elements and an order of $N = 10$ was chosen. The location of the outer boundaries at $l_i = 70D$, $l_b = 70D$, $l_o = 50D$ results in an error of about 0.5% compared to a solution with very large boundary extensions.

Integral forces on the cylinder are used in order to compare different configurations. Besides the pressure and the frictional part, the force definition has been extended by the electromagnetic thrust ($-C_{EMx}$), expressing a measurable force on the cylinder if the flow was at rest. We define the drag force as

$$F_D = F_{D_f} + F_{D_p} + F_{D_{em}} = \oint_S \mu \frac{\partial U_t}{\partial n_y} \mathrm{d}S - \oint_S P n_x \, \mathrm{d}S - J_0 B_0 \frac{a}{\pi} D(\cos\phi_0 - \cos\phi_1) \tag{10}$$

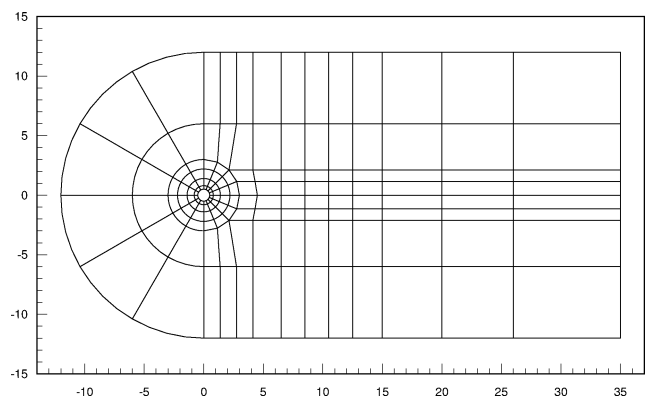

Figure 4. Spectral element mesh around the circular cylinder.

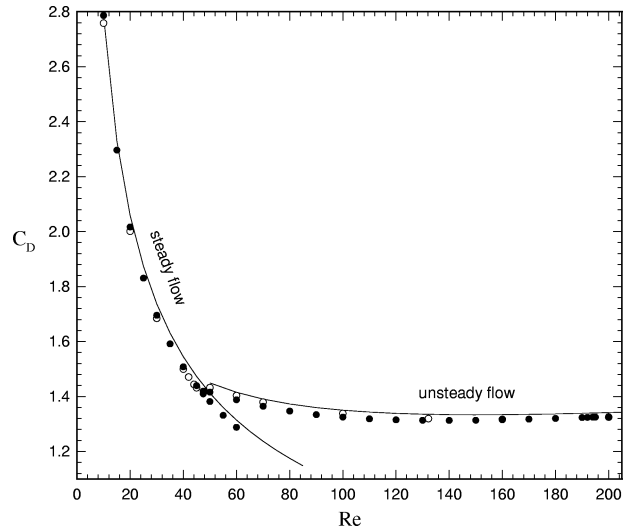

Figure 5. Results of drag versus Reynolds number compared to numerical works: ——, Henderson [13]; ○, Lange [14]; ●, present work.

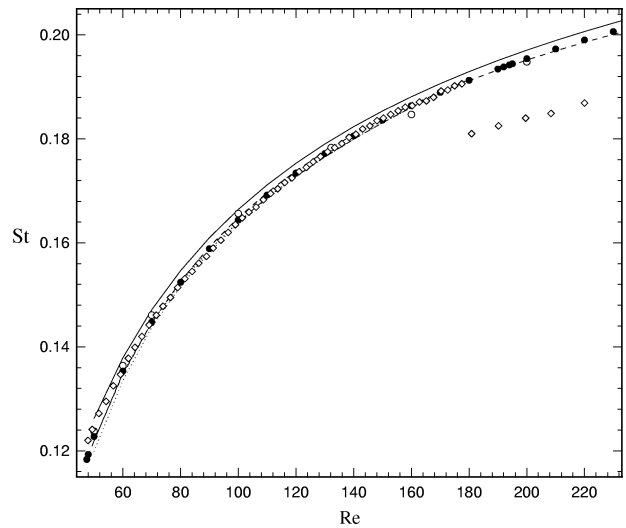

Figure 6. Variation of Strouhal number with Reynolds number: ——, Henderson [13]; ○, Lange [14]; ●, present work (numerics); – – –, Fey [15]; ·····, Leweke and Provansal [16]; –·–·–, Norberg [17]; ◇, Williamson [18] (experiments).

with U_t the tangential velocity, P the wall pressure, and n_x, n_y are the x- and y-components of the normal vector to the cylinder surface S. The drag coefficient is defined as follows

$$C_D = \frac{F_D}{\frac{1}{2}\rho U_\infty^2 D}. \tag{11}$$

A nondimensional quantity to compare the results with experiments is the frequency of vortices in the unsteady wake, called Strouhal number, defined as

$$St = \frac{f D}{U_\infty}, \tag{12}$$

where the diameter D is used as characteristic length. The frequency f has been measured from the unsteady lifting force.

In order to validate the code, two-dimensional calculations have been performed for $10 \leqslant Re \leqslant 230$, and compared to the numerical works of Henderson [13], Lange [14] as well as measurements of Fey [15], Leweke and Provansal [16], Norberg [17], and Williamson [18]. *Figure 5* shows the drag curve for the two-dimensional cylinder flow. The agreement between this work, and the results of Lange and Henderson is very good, except that the curve of the latter is slightly shifted to higher values because of blockage effects. Experimental values for the drag are not considered here, because of the large scatter in published results due to difficulties in measurements of very small forces. In the low Reynolds number regime, as considered here, the significance of pressure drag increases with Reynolds number. At $Re = 10$, the pressure drag makes up 57% of total drag, whereas at $Re = 200$ it contributes about 81%. The correspondence to the measured Strouhal numbers St is excellent as shown in *figure 6*. The deviation between the results lies in the order of experimental errors. Henderson kept again higher values due to the smaller computational domain. Note that the experimental curves drop for $Re \approx 180$ because of a transition to three-dimensionality and deviate from two-dimensional numerical results. Fey [15] could sustain a two-dimensional cylinder flow until $Re \approx 230$ by means of two thin wires, tightened parallel to the cylinder axis at $x/D = 1.05$, $\phi = \pm 174°$. His measurements confirm the 2D calculations for $Re > 180$.

4. Effects of EMFC on the cylinder flow at a constant Reynolds number

The flow around a cylinder can be controlled by a tangentially applied Lorentz force that accelerates the flow near the wall. Fundamental effects are shown at a Reynolds number of $Re = 200$ ($G = 0.5$), where the flow is characterized by the von Kármán vortex street. An increasing interaction parameter (Lorentz force) results in a stabilization of the flow around the cylinder as shown in *figure 7*. The uncontrolled case ($N = 0$) is compared to medium forces ($N = 0.8$ and $N = 1.2$) and a strong force ($N = 6.0$). The latter corresponds to a negative total

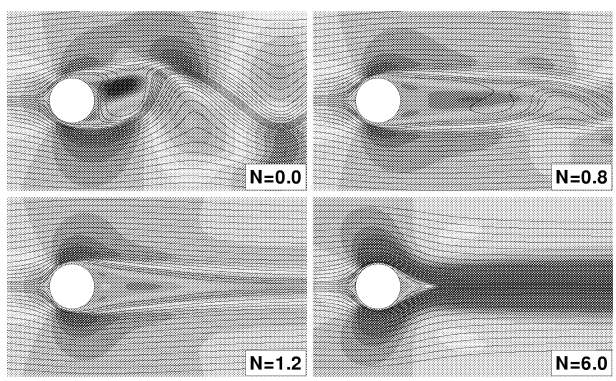

Figure 7. Contours of streamwise velocity and streamlines for the flow at varied interaction parameter ($Re = 200$). The dark color near the cylinder wall and in the wake at $N = 6.0$ indicates the flow acceleration.

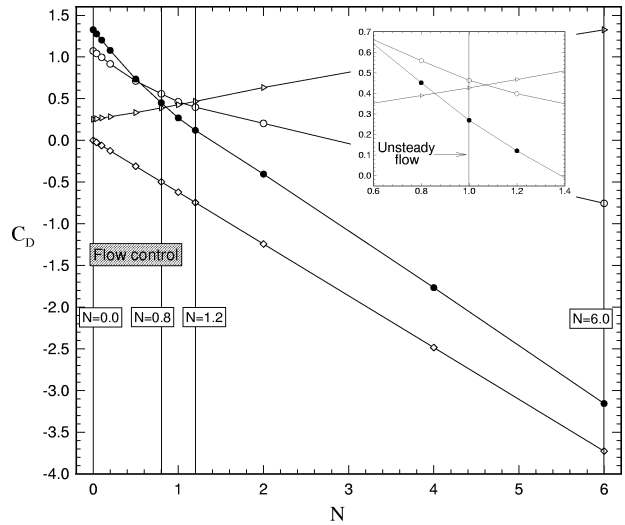

Figure 8. Dependence of drag coefficients on interaction parameter at $Re = 200$: ○, C_{Dp}; ▷, C_{Df}; ◇, C_{EMx}; ●, C_D.

drag that is practically a MHD-propulsion. We are mostly interested in the small and medium force regime in terms of flow control.

In the following, it is shown how this qualitative views are expressed in quantitative force coefficients. *Figure 8* contains results of calculations at $Re = 200$ for the pressure C_{Dp} and frictional drag C_{Df}, electromagnetic thrust C_{EMx}, and total drag C_D. It can be seen that the frictional drag increases with larger interaction parameters, whereas the other coefficients decrease. The nearly linear drag curves have a kink at $N \approx 1.0$ corresponding to the transition from an unsteady flow to a steady state (see *figure 8* insert). This has been shown qualitatively in *figure 7*. The displayed points are included in *figure 8*. The area that is interesting for flow control is also shown in the figure. If the total drag is lower than zero, we enter the region of MHD-propulsion because the cylinder would be accelerated by the Lorentz force.

4.1. Results for low and moderate interaction parameters

Since calculations in the unsteady flow regime ($Re > 47$) are very time-consuming, the studies have been proceeded at a Reynolds number of $Re = 40$. First, the optimal location of the electromagnetic system at the cylinder surface is searched in order to minimize the input of electrical current density. For this, the cylinder was covered with the em-system in steps of $\Delta\phi = 10°$ in the azimuthal direction (the angle ϕ is defined in *figure 3*). The first calculation starts with an em-system from 0° to 10° (350° to 360° at the lower half of the cylinder), where the variation of drag with interaction parameter is determined. Then, the cylinder is covered from 10° to 20° and so on, until 170° to 180°. The em-system has been mirrored to the lower half of the cylinder in all cases. Altogether, 18 runs have been performed per interaction parameter. The change of total drag with increasing interaction parameter has been measured and is shown in *figure 9*. It can be seen that an induction of the Lorentz force prior to 90° considerably increases the drag coefficient. The flow is accelerated at the wall, the minimum pressure at $\phi \approx 90°$ is further decreased, and the flow separation is shifted towards the front stagnation point. Together with the increase of the skin friction, the total drag increases. Applied at angles higher than 90°, the force causes a postponement of flow separation and a decrease in pressure drag. The optimal location of Lorentz force induction is visible in the picture. A control of flow between 120° and 140° is most efficient. This locations correspond to the point of flow separation at $\phi \approx 125°$ for $Re = 40$.

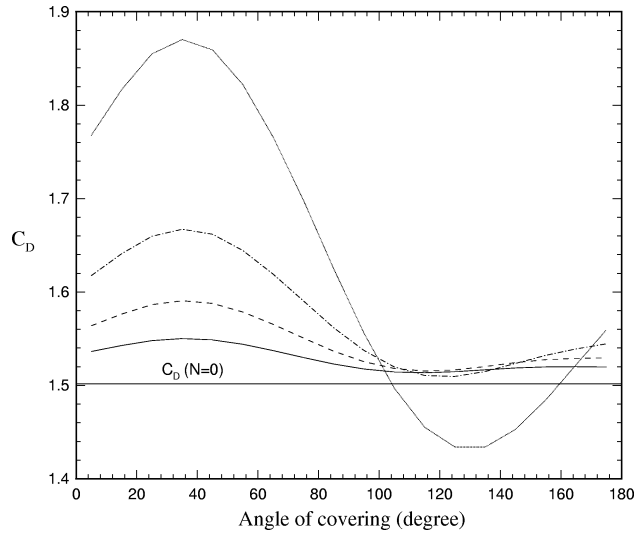

Figure 9. Variation of total drag with location of Lorentz force actuation at different interaction parameters ($Re = 40$): ——, $N = 0.5$; – – –, $N = 1.0$, –·–·–; $N = 2.0$; ·····, $N = 5.0$.

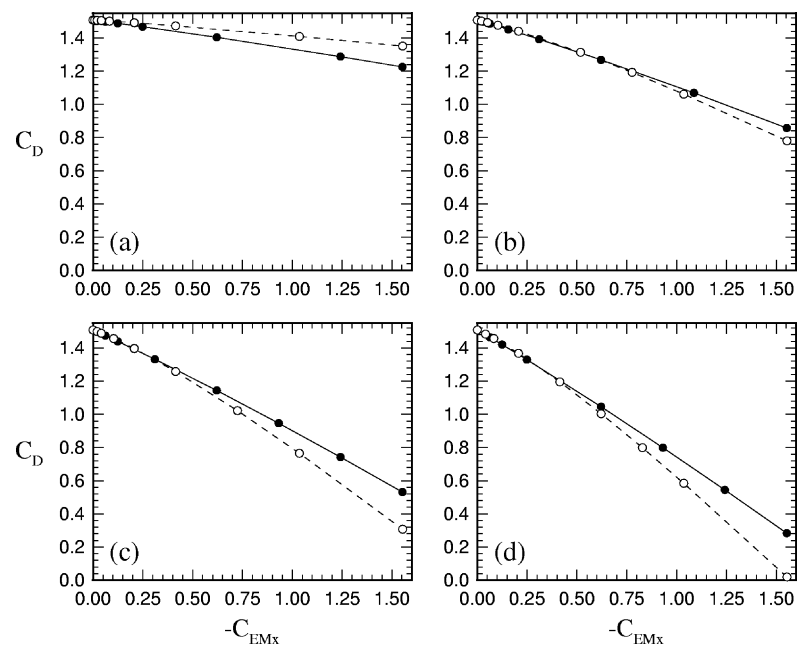

Figure 10. Total drag versus electromagnetic thrust for $Re = 40$: (a) $G = 0.1$; (b) $G = 0.25$; (c) $G = 0.5$; (d) $G = 1.0$ (——, 12°–168°; – – –, 100°–150°).

Based on the optimum location of EMFC, two configurations were chosen for further investigations: (1) induction of the Lorentz force from 12° to 168° used in the experiments by Weier et al. [10]; and (2) an optimized configuration with a force from 100° to 150°. Again, a stationary flow regime has been studied ($Re = 40$), and the interaction parameter N as well as the geometry parameter G have been varied. Changes in the force profile for different geometry parameters (widths of electrodes/magnets) are shown

in *figure 2*. The integral Lorentz force $-C_{EMx}$, denoted as electromagnetic thrust, is used to compare the different configurations. *Figure 10* shows the total drag versus electromagnetic thrust at geometry parameters $G = 0.1, 0.25, 0.5,$ and 1.0 (solid lines 12°–168°, dashed lines 100°–150°). Only a modest drag reduction is possible with a small geometry parameter. These is even worse in the 100° to 150° case. The behavior changes if medium or higher values $G \geqslant 0.25$ are concerned. The optimized configuration results in a larger drag reduction. *Table I* shows some quantitative values for the maximal electromagnetic thrust calculated. The influence of the geometry parameter on drag reduction is significant. It differs between nearly 10% and 100% at this Reynolds number. The Reynolds number dependence of reduction is presented in section 5. Furthermore, pressure and frictional drag are shown versus geometry parameter and electromagnetic thrust (see *figure 11*). The pressure drag is reduced due to the Lorentz force. A strong decrease occurs in the 100° to 150° case compared to the original configuration, where the flow acceleration on the front part of the cylinder lowers the pressure minimum at $\phi \approx 90°$, and the separation is shifted to lower angles, if this was not compensated by the force at the rear part. As expected, the frictional drag decreases towards higher geometry parameters, since the Lorentz force profile (equation (5)) flattens. Therefore, the flow acceleration near the wall is diminished with higher values of G. The optimized version has a larger frictional drag in all cases. This results from the strong

Table I. Effect of geometry parameter on drag reduction at maximal electromagnetic thrust.

G	12°–168°	100°–150°
0.10	18.7%	10.4%
0.25	43.1%	48.3%
0.50	64.8%	79.6%
1.00	81.2%	98.7%

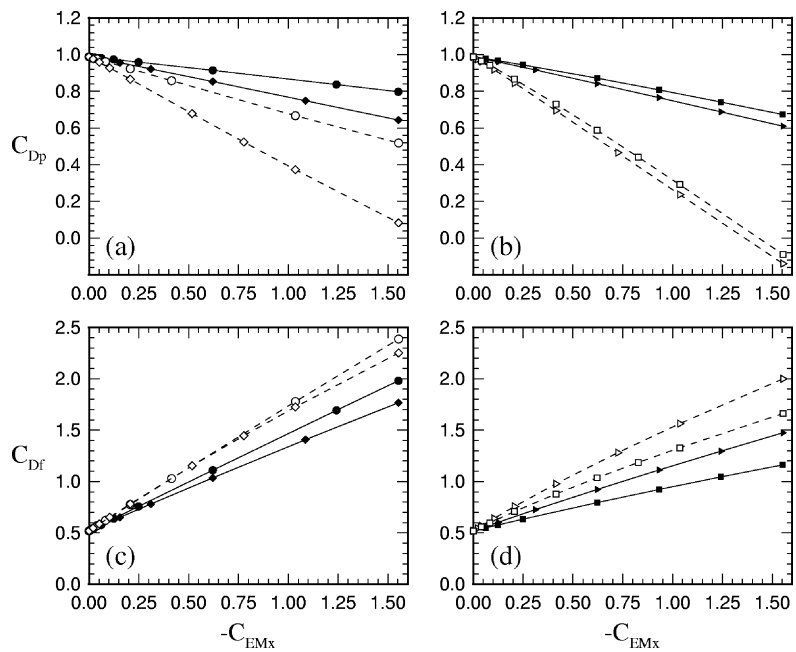

Figure 11. Pressure (top) and frictional drag (bottom) versus electromagnetic thrust for $Re = 40$: ○, $G = 0.1$; ◇, $G = 0.25$; ▷, $G = 0.5$; □, $G = 1.0$ (——, 12°–168°; – – –, 100°–150°).

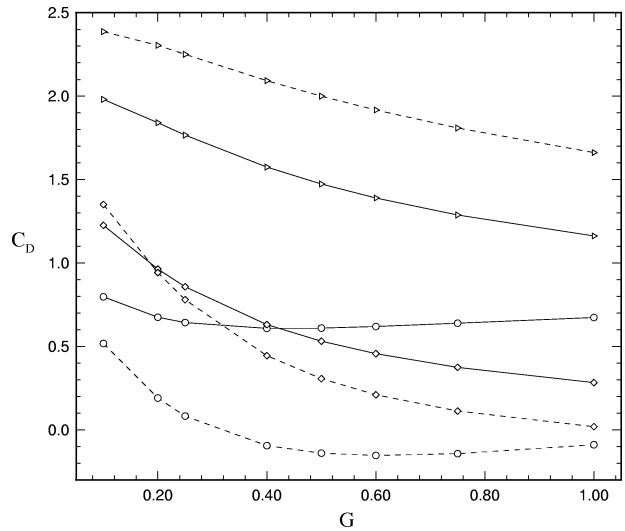

Figure 12. Dependence of pressure, frictional, and total drag on geometry parameter at maximal electromagnetic thrust for $Re = 40$: ○, C_{Dp}; ▷, C_{Df}; ◇, C_D; (——, 12°–168°; – – –, 100°–150°).

Lorentz force (large interaction parameter) in a small area of the surface, where the skin friction is low without force due to the boundary layer separation.

Since the drag reduction increases with higher geometry parameters, the question after an optimum has been posed. In *figure 12*, we show the variation of drag coefficients with geometry parameter at the largest electromagnetic thrust calculated. The total drag declines with increasing G, but the slope of the curve is lowered. At $G = 1.0$, the drag curve shows nearly no diminution, since both configurations have a pressure drag minimum at medium geometry parameters (12°–168°: $G = 0.4$, 100°–150°: $G = 0.6$), whereas the frictional drag is further decreased.

4.2. Results for large interaction parameters

In order to complete the view on electromagnetic flow control, calculations have been performed for very large interaction parameters at a constant Reynolds number ($Re = 40$). The investigation was targeted at a revelation of fundamental physical changes in that regime. *Figure 13* shows the results for different geometry parameters. The scaled interaction parameter $N \cdot G$ is plotted in order to compare the calculations at various G. It can be seen that the slope of all curves steepens, since the Lorentz force becomes the dominant part of total drag. The curves further disperse at larger forces due to the nearly linear increase in frictional drag. The case $G = 1.0$ is most efficient for drag reduction and MHD-propulsion in the infinite limit. We have included the main area of interest for flow control purposes in the figure, where the drag is reduced between 10% and 50%. For the largest interaction parameters at $G = 0.25$ to $G = 1.0$, no steady solutions have been obtained. The strong Lorentz force generates a jet in the cylinder wake that starts to oscillate. Time-dependent drag and lifting forces have been observed on the cylinder. It should be noted that it remains unclear whether two-dimensional calculations are able to reflect the physics of this jet and of its instability. Further investigations are beyond the scope of the paper.

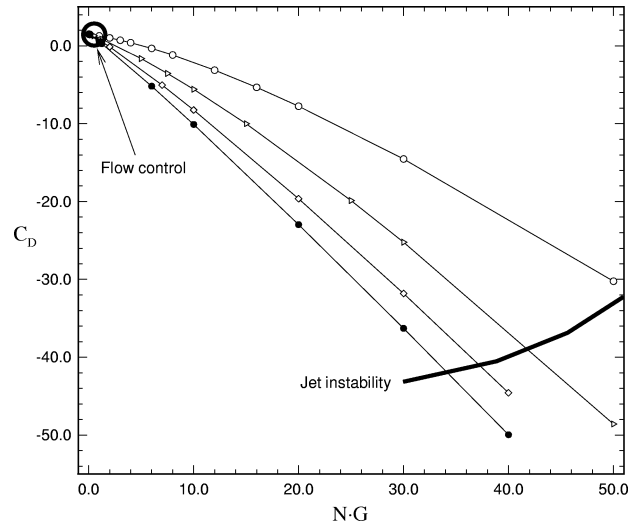

Figure 13. Drag coefficient versus interaction parameter at $Re = 40$: ○, $G = 0.1$; ▷, $G = 0.25$; ◇, $G = 0.5$; ●, $G = 1.0$ (electrodes/magnets 12°–168°).

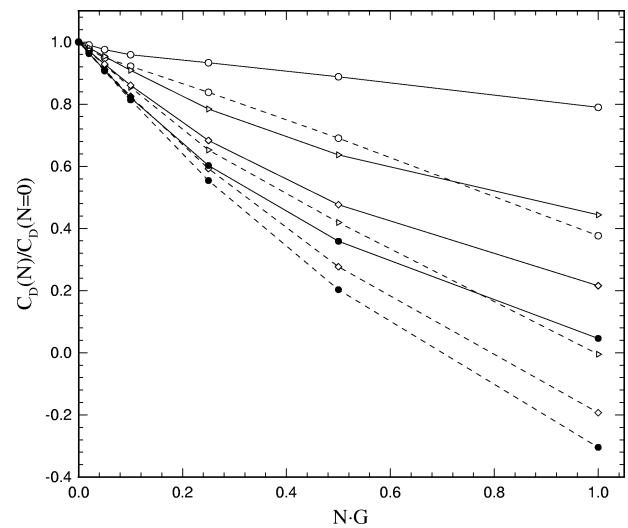

Figure 14. Variation of normalized total drag with scaled interaction parameter for different Reynolds numbers: ○, $Re = 50$; ▷, $Re = 100$; ◇, $Re = 150$; ●, $Re = 200$ (——, $G = 0.1$; – – –, $G = 0.5$).

5. Reynolds number dependence of EMFC

In the following, we will tackle the question after the behavior at increasing Reynolds numbers and in the unsteady flow regime. It is supposed that the effect of EMFC increases also for smaller geometry parameters (penetration depths) due to the decreasing boundary layer thickness. Various calculations have been performed for $G = 0.1$, where a very modest drag decrease was observed at $Re = 40$, and $G = 0.5$ at Reynolds numbers of $Re = 50, 100, 150,$ and 200. Only the original configuration, with an em-system from 12° to 168°, has been considered. *Figure 14* shows the effect of scaled interaction parameter on total drag. The solid lines denote results for $G = 0.1$ and the dashed lines for $G = 0.5$. An increasing Reynolds number results in a steeper gradient in terms of drag reduction for the $G = 0.5$ case. It can be seen that the drag reduction mechanism has

Table II. Variation of drag reduction with Reynolds number ($N \cdot G = 1.0$).

Re	$G = 0.5$	$G = 0.1$
50	62.3%	21.0%
100	100.5%	55.6%
150	119.3%	78.4%
200	130.5%	95.4%

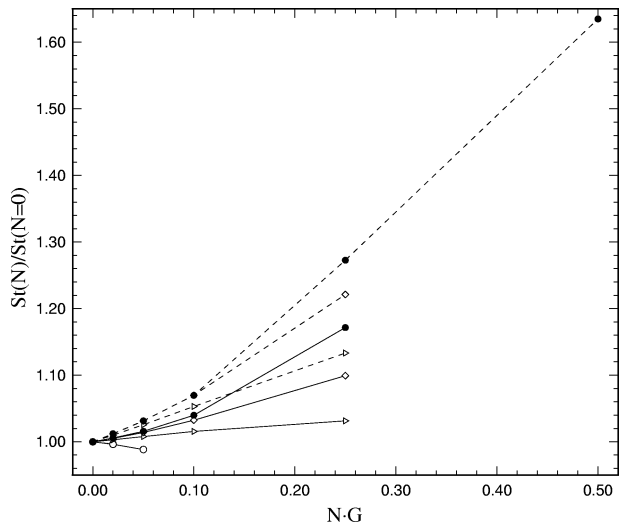

Figure 15. Variation of normalized Strouhal number with scaled interaction parameter for different Reynolds numbers: ○, $Re = 50$; ▷, $Re = 100$; ◇, $Re = 150$; ●, $Re = 200$ (——, $G = 0.1$; – – –, $G = 0.5$).

an improved efficiency at larger Reynolds numbers. Calculations with the smaller geometry parameter $G = 0.1$ have shown only a slight drag decrease at lower Reynolds numbers $Re = 50$ and $Re = 100$, whereas the drag reduction is increased towards higher *Re*.

The increasing drag reduction with rising Reynolds number can be explained by looking at the drag components. At the largest interaction parameter calculated and $G = 0.5$, the frictional drag is increased by 157% at $Re = 50$ versus 150% at $Re = 200$ (the absolute value is nearly two times higher at $Re = 50$), whereas the pressure drag is reduced by 38% and 81% respectively (nearly equal absolute values). This results in a reduction of total drag of 62% at $Re = 50$ and 130% at $Re = 200$ (see *table II*). Since the pressure drag dominates the drag coefficient at higher Reynolds numbers and the boundary layer is thinning, the effect of EMFC increases at constant energy input. This is limited by the transition to turbulence of the boundary layer at $Re \approx 10^5$. Here, a strong decay of total drag is noted due to the drop in pressure drag. The dominating frictional drag leads to a questionable application of a streamwise Lorentz force for the purpose of drag reduction at high Reynolds numbers.

An other interesting value of bluff body flows is the frequency of vortex shedding, nondimensional expressed as Strouhal number (see equation (12)). The change of Strouhal numbers with increasing interaction parameter at different Reynolds numbers is shown in *figure 15* for $G = 0.1$ and $G = 0.5$. At $Re = 50$ and $G = 0.5$, the flow has been stabilized after the first interaction parameter calculated, so only a steady solution has been obtained. The Strouhal number grows with increasing forcing and Reynolds numbers. This effect is stronger for $G = 0.5$ than for $G = 0.1$. The vortex shedding is accelerated by the streamwise Lorentz force that acts as an artificial

increasing of the Reynolds number by inducing additional momentum. The increase of the Strouhal number is visible in the wake by two phenomena: (1) the streamwise distance of vortices is diminished; and (2) the vortices remain closer to the symmetry line and oscillate more weakly.

The effect of the Lorentz force on the velocity distribution in the flow field is considered at $Re = 40$ (steady flow) and $Re = 200$ (unsteady flow). Again, two different geometry parameters $G = 0.1$, inducing a strong near-wall force and fast decay of the exponential force profile, and $G = 0.5$, connected with a lower near-wall force and modest decay into the flow, has been chosen. First, the change of tangential velocity normal to the wall under the influence of the Lorentz force is investigated. The scaled interaction parameter was set to $N \cdot G = 0.1$, corresponding to a weak force, and to $N \cdot G = 1.0$, inducing a stronger force. As shown in *figure 16* and *17*, the velocity profiles are nearly identical for the weak forcing. The left graphs, marked by (a), shows the velocity at $\phi = 90°$. The force accelerates the flow and the velocity profile becomes fuller that means more stable. Differences between the parameters $G = 0.5$ and $G = 0.1$ are bigger at $Re = 40$. At $G = 0.1$, the flow is only forced in regions of dominating skin friction because of the thicker boundary layer that reduces the EMFC effectiveness. The smaller boundary layer thickness at $Re = 200$ leads to an equally controlled flow in both cases.

The velocity profiles at the second position considered $\phi = 150°$ (see *figure 16(b)* and *17(b))* clearly indicate the separated flow, if the force is weak. The velocity gradient at the wall $\frac{\partial U_t}{\partial \mathbf{n}}|_{r=0}$ is negative and has an inflectional point away from the wall indicating a highly unstable velocity profile. Both cases ($G = 0.5$ and $G = 0.1$) result in a flow stabilization at the smaller Reynolds number $Re = 40$ for sufficiently large Lorentz forces ($N \cdot G = 1.0$). Again, the higher force at the wall for $G = 0.1$ accelerates the flow with a local maximum in the velocity profile near the wall. By way of contrast, the induced Lorentz force at $Re = 200$ is not able to generate a positive velocity gradient at the wall for $G = 0.5$. The impact of the force appears at first away from the cylinder surface, where the velocity profile becomes fuller. The strong force at the wall for $G = 0.1$ prevents the flow separation on $\phi = 150°$, so that the pressure drag is reduced considerably. The reduction in total drag is smaller than for $G = 0.5$ because of the strong increase in the frictional drag (more than three times compared to the noncontrolled case).

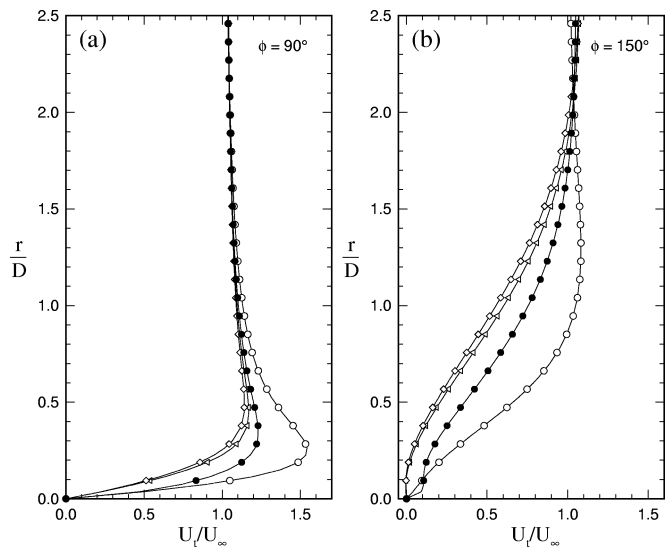

Figure 16. Tangential velocity normal to the wall of the circular cylinder at $Re = 40$: ◁, $G = 0.5$, $N \cdot G = 0.1$; ○, $G = 0.5$, $N \cdot G = 1.0$; ◇, $G = 0.1$, $N \cdot G = 0.1$; ●, $G = 0.1$, $N \cdot G = 1.0$; (a) $\phi = 90°$, (b) $\phi = 150°$.

Moreover, the streamwise velocity U/U_∞ in the wake of the cylinder is plotted for $Re = 40$ in *figure 18* and $Re = 200$ in *figure 19* ($G = 0.1$ and $G = 0.5$). The magnitude of the depression in the velocity profile is directly connected to the drag on the cylinder. However, an integration of wall forces is more exact compared to that method. The depression becomes wider with increasing distance from the cylinder, and the mean velocity decreases. If the Lorentz force is weak, a reversed flow still occurs at $x/D = 1.5$ (see graphs (a)) at both Reynolds numbers. The velocity maxima from the shear layer are easily seen in the figure. The low velocity at the centerline indicates that the drag is only slightly decreased. Calculations by means of the stronger Lorentz force show the velocity increase in the near-wake. The drag reduction becomes obvious from these curves.

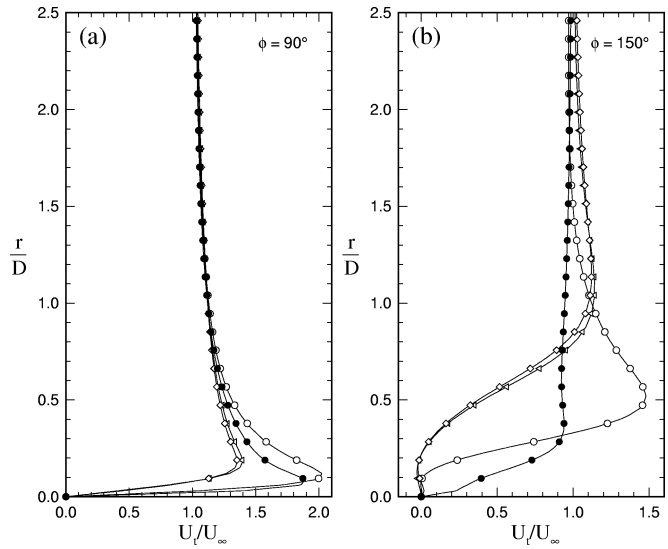

Figure 17. Tangential velocity normal to the wall of the circular cylinder at $Re = 200$: ◁, $G = 0.5$, $N \cdot G = 0.1$; ○, $G = 0.5$, $N \cdot G = 1.0$; ◇, $G = 0.1$, $N \cdot G = 0.1$; ●, $G = 0.1$, $N \cdot G = 1.0$; (a) $\phi = 90°$, (b) $\phi = 150°$.

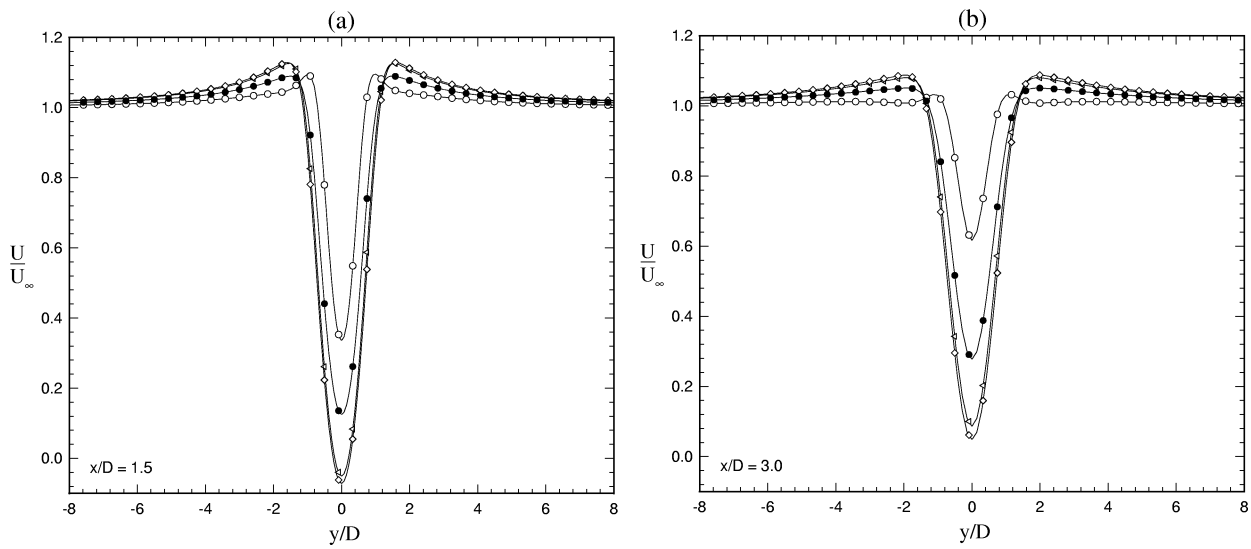

Figure 18. Streamwise velocity at different positions in the wake of the circular cylinder at $Re = 40$: ◁, $G = 0.5$, $N \cdot G = 0.1$; ○, $G = 0.5$, $N \cdot G = 1.0$; ◇, $G = 0.1$, $N \cdot G = 0.1$; ●, $G = 0.1$, $N \cdot G = 1.0$; (a) $x/D = 1.5$, (b) $x/D = 3.0$.

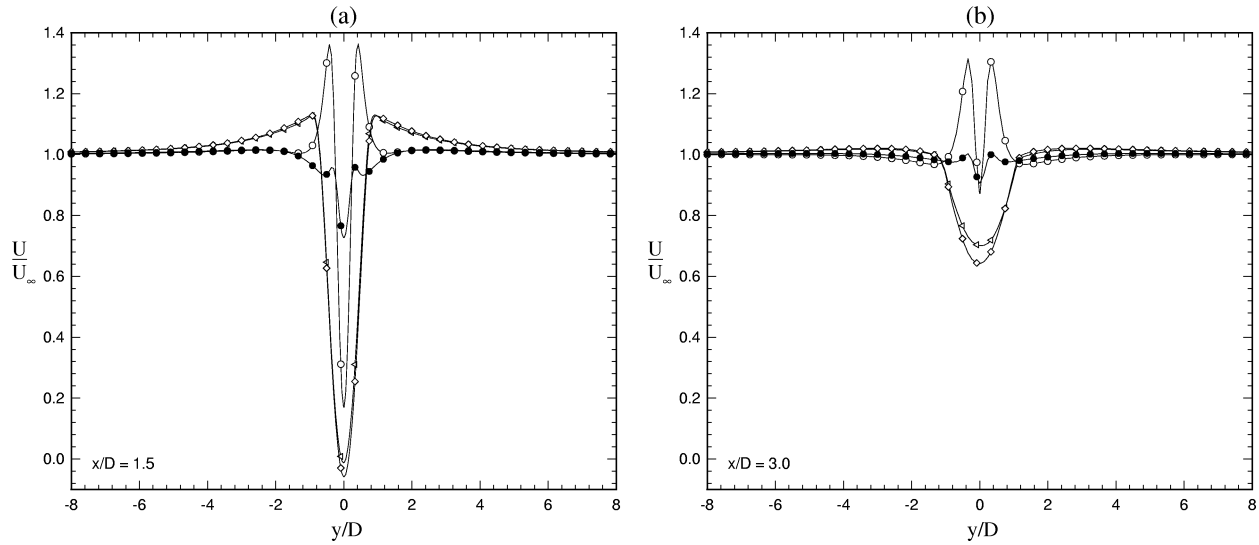

Figure 19. Streamwise velocity at different positions in the wake of the circular cylinder at $Re = 200$: ◁, $G = 0.5$, $N \cdot G = 0.1$; ○, $G = 0.5$, $N \cdot G = 1.0$; ◇, $G = 0.1$, $N \cdot G = 0.1$; ●, $G = 0.1$, $N \cdot G = 1.0$; (a) $x/D = 1.5$, (b) $x/D = 3.0$.

At $Re = 40$, plotted in *figure 18(a)*, the velocity minimum is lower for $G = 0.1$ than for $G = 0.5$, and the drag decrease is diminished. *Figure 19(a)* shows an opposite behavior, as the centerline velocity is larger for $G = 0.1$ compared to $G = 0.5$, but the second case shows striking velocity maxima and a stronger decrease in drag. This maxima acts like jets in the wake of the circular cylinder. If the geometry parameter is small ($G = 0.1$), only modest peaks occur, since the Lorentz force is effective in a region of large shear-stress. At the position $x/D = 3.0$ the same appearances can be observed (see graph (b) of *figure 18* and *figure 19*). No reversed flow is detected, but the drag increase due to the lower velocity maxima for $G = 0.1$ at $Re = 40$ and structures similar to jets for $G = 0.5$ at $Re = 200$ remain significant characteristics. This velocity peaks do not appear at $Re = 40$. Because of the thicker boundary layer, the Lorentz force induction is compensated by the viscous forces, whereas at $Re = 200$ an effective magnitude of the force acts in the outer part of the boundary layer. The relation between boundary layer thickness and shape of the Lorentz force profile could be extended to a criterion for the minimum geometry parameter to control the flow at higher Reynolds numbers.

6. Postponement of instability of the stationary flow

If the Reynolds number exceeds a critical value Re_C, the stationary flow, characterized by two symmetrical vortices in the near wake due to flow separation, passes into a time-dependent flow regime, and it develops the well-known von Kármán vortex street. This primary instability of cylinder flow results from a global Hopf bifurcation of the steady flow. A critical Reynolds number $Re_{C_1} = 46.72$ has been obtained from the intersection of the steady and unsteady drag curves. It agrees well with values from a stability analysis by Jackson [19] $Re_{C_1} = 46.184$ and experiments (see Fey [15]) $Re_{C_1} \approx 47$.

In this section, the influence of the Lorentz force on the first critical Reynolds number is shown. Two-dimensional calculations have been performed at $60 \leqslant Re \leqslant 300$ under a variation of the interaction parameter N. The cylinder surface has been covered with electrodes and magnets from 12° to 168°. The geometry parameter has been set to $G = 0.2$ (experiments of Weier et al. [10]) and $G = 0.4$ in order to investigate its impact of the Lorentz force profile. Runs have been started from a steady solution, where the flow field

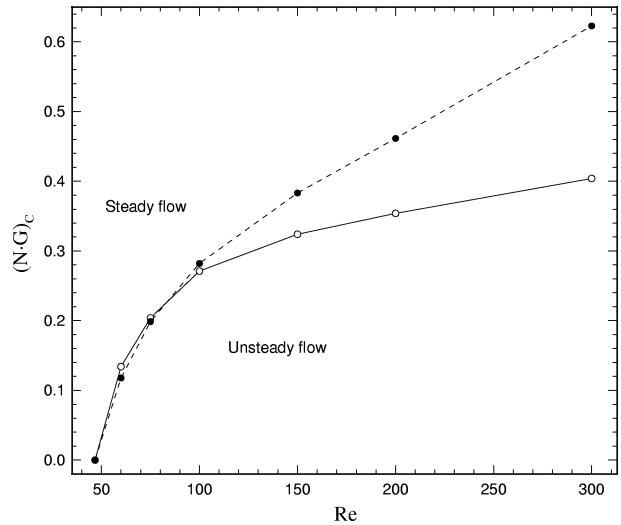

Figure 20. Dependence of stability of two-dimensional flow on Reynolds numbers under the influence of Lorentz forces for different geometry parameters: ——, $G = 0.2$; – – –, $G = 0.4$.

was perturbed for a short period. Then the amplification of perturbations has been determined. Afterwards, we have increased the interaction parameter to obtain a negative amplification that points at a stable flow. A simple interpolation leads to the critical $(N \cdot G)_C$ as shown in *figure 20*. Again, we have used the scaled interaction parameter in order to compare the two configurations under the same energetical input. As expected, the critical interaction parameter grows with Reynolds number and achieves rather high values for the maximum *Re* considered. The suppression of lifting forces on bluff bodies requires a considerable amount of electrical current density on the electrodes. A practical application of the complete elimination of oscillating forces remains out of sight if the electromagnetic thrust, necessary to suppress the vortex street, is compared to the achieved drag reduction of approximately 50% at $Re = 200$. As it can be seen in *figure 20*, the curves $G = 0.2$ and $G = 0.4$ agree very well for $Re \leqslant 100$. At larger Reynolds numbers, the curves deviate considerably. The result that the flow is stabilized at lower Lorentz forces for $G = 0.2$ compared to $G = 0.4$ has not been expected from the preceding investigations where the drag reduction is enlarged with increasing geometry parameter. It is supposed from *figure 19* that the peaks in the velocity profile destabilize the flow, whereas a Lorentz force in the region of high shear-stresses acts stabilizing.

It is questionable whether this considerations are valid beyond the point of the secondary instability, where the cylinder wake becomes three-dimensional ($Re_{C_2} \approx 190$). But if we suppose that the secondary instability is weaker than the primary one and realize an ideal force profile without spanwise variations, then the three-dimensional structures are suppressed together with the vortex street. Investigations at higher Reynolds numbers to clear this question are beyond the aim of this paper.

7. Conclusions

The flow around a circular cylinder at low Reynolds numbers under the influence of electromagnetic forces was studied by means of two-dimensional numerical simulations. Stripes of electrodes and magnets induce crossed fields that generate a Lorentz force tangential to the cylinder surface. The force is exponentially decaying in the wall-normal direction and acts mainly near the wall. This mechanism even works at low electrical conductivities e.g. in seawater. The body force stabilizes the flow by a prevention of development of an

inflectional velocity profile. So the flow separation is postponed and the pressure drag decreases considerably. By way of contrast, the frictional drag is increased due to an acceleration of fluid near the wall.

How this mechanism results in a decay of total drag, strongly depends on the location of force induction and on the shape of the Lorentz force profile that is determined by the width of electrodes and magnets expressed as geometry parameter. The optimal location of control was found in the region just before and after flow separation. The dependence of drag reduction on Reynolds number and geometry parameter was studied. It was shown that the impact of EMFC is influenced by a correlation between the force profile and the boundary layer thickness. Moreover, we showed that the suppression of the von Kármán vortex street is possible through the Lorentz force. It depends again on the geometry parameter and on the interaction parameter.

It has become clear that the interaction parameter, as used in literature about EMFC, is not sufficient to describe the effect of flow control in order to compare different works. The shape of the exponentially decaying force profile is responsible for possible reductions of drag of the circular cylinder.

Applications of EMFC in the area of moving vehicles in seawater require the investigation of flows at higher Reynolds numbers. Three-dimensionality as well as turbulent boundary layers and wakes are the fundamental characteristics of that flows. The further work has to be concentrated on that topics.

Acknowledgments

We thank Professor G.E. Karniadakis (Brown University, Providence, USA) for the donation of the spectral element code and our colleagues at the research center ‘Forschungszentrum Rossendorf’ for their advice. The support of Deutsche Forschungsgemeinschaft (DFG INK 18 B1-1 TP A2) is gratefully acknowledged, and we want to thank the Center for High-Performance Computing of Dresden University of Technology for providing extensive computational resources.

References

[1] Gailitis A., Lielausis O., On a possibility to reduce the hydrodynamical resistance of a plate in an electrolyte, Appl. Magnetohydrodyn., Rep. of the Phys. Inst. Riga 12 (1961) 143–146 (in Russian).
[2] Tsinober A., MHD flow drag reduction, in: Bushnell D.M., Hefner J.N. (Eds.), Viscous Drag Reduction in Boundary Layers, Progress in Astronautics and Aeronautics, Vol. 123, American Institute of Aeronautics and Astronautics, 1989, pp. 327–349.
[3] Nosenchuck D.M., Brown G.L., The direct control of wall shear-stresses in a turbulent boundary layer, in: So R.M.C., Speziale C.G., Launder B.E. (Eds.), Proc. of the Intern. Conf. on Near-Wall Turbulent Flows, Elsevier, 1993, pp. 689–698.
[4] Henoch C., Stace J., Experimental investigation of a salt water turbulent boundary layer modified by an applied streamwise magnetohydrodynamic body force, Phys. Fluids 7 (6) (1995) 1371–1383.
[5] Crawford C.H., Karniadakis G.E., Reynolds stress analysis of EMHD-controlled wall turbulence. Part I. Streamwise forcing, Phys. Fluids 9 (3) (1997) 788–806.
[6] Fan X., Brown G.L., Experiments on the electromagnetic control of turbulence, AIAA-Paper 97-2123, 1997.
[7] O’Sullivan P.L., Biringen S., Direct numerical simulation of low Reynolds number turbulent channel flow with EMHD control, Phys. Fluids 10 (5) (1998) 1169–1181.
[8] Berger T.W., Kim J., Lee C., Lim J., Turbulent boundary layer control utilizing the Lorentz force, Phys. Fluids 12 (3) (2000) 631–649.
[9] Weier T., Gerbeth G., Mutschke G., Platacis E., Lielausis O., Experiments on the cylinder wakes stabilization in an electrolytic solution by means of electromagnetic forces localized on the cylinder surface, Exp. Therm. Fluid Sci. 16 (1998) 84–91.
[10] Weier T., Gerbeth G., Mutschke G., Fey U., Posdziech O., Lielausis O., Platacis E., Some results on electromagnetic control of flow around bodies, in: Proc. of the Intern. Symp. on Seawater Drag Reduction, Newport, Rhode Island, 1998, pp. 395–400.
[11] Karniadakis G.E., Israeli M., Orszag S.A., High-order splitting methods for the incompressible Navier–Stokes equations, J. Comp. Phys. 97 (1991) 415–443.
[12] Henderson R.D., Karniadakis G.E., Unstructured spectral element methods for simulation of turbulent flows, J. Comp. Phys. 122 (1995) 191–217.
[13] Henderson R.D., Details on the drag curve near the onset of vortex shedding, Phys. Fluids 7 (9) (1995) 2102–2104.

[14] Lange C., Numerical predictions of heat and momentum transfer from a cylinder in crossflow with implications to hot-wire anemometry, Diss., Univ. Erlangen-Nürnberg, Germany, 1997.
[15] Fey U., Eine neue Gesetzmäßigkeit für die Wirbelfolgefrequenz des Kreiszylinders und Steuerung der Instabilitäten im Bereich $160 < Re < 300$, MPI für Strömungsforschung, Rep. No. 3/1998, Göttingen, 1998.
[16] Leweke T., Provansal M., The flow behind rings: bluff body wakes without end effects, J. Fluid Mech. 288 (1995) 265–310.
[17] Norberg C., An experimental investigation of the flow around a circular cylinder: influence of aspect ratio, J. Fluid Mech. 258 (1994) 287–316.
[18] Williamson C.H.K., Oblique and parallel modes of vortex shedding in the wake of a circular cylinder at low Reynolds numbers, J. Fluid Mech. 206 (1989) 579–627.
[19] Jackson C.P., A finite-element study of the onset of vortex shedding in flow past variously shaped bodies, J. Fluid Mech. 182 (1987) 23–45.